Perovskite-Type Solid Solution Nano-Electrocatalysts Enable Simultaneously Enhanced Activity and Stability for Oxygen Evolution

*Xiao Liang, Lei Shi, Rui Cao, Gang Wan, Wensheng Yan, Hui Chen, Yipu Liu, and Xiaoxin Zou**

A trade-off between catalytic activity and structural stability generally exists in oxygen evolution electrocatalysis, especially in acidic environment. This dilemma limits the development of higher-performance electrocatalysts that are required by next-generation electrochemical technologies. Here it is demonstrated that the inverse catalytic activity–structural stability relation can be broken by alloying catalytically inert strontium zirconate with the other catalytically active perovskite, strontium iridate. This strategy results in an alloyed perovskite electrocatalyst with simultaneously improved iridium mass activity and structural stability, by about five times, for the oxygen evolution reaction under acidic conditions. The experimental and theoretical results suggest that the alloying strategy generates multiple positive effects, mainly including the reduction of catalyst size, the decrease of catalyst covalency, and the weakening of surface oxygen-binding ability. The synergistic optimization of bulk and surface properties, as a result, enhances the intrinsic activity and availability of surface iridium sites, whilst significantly inhibiting the surface cation corrosion during electrocatalysis.

X. Liang, L. Shi, Dr. H. Chen, Dr. Y. Liu, Prof. X. Zou
State Key Laboratory of Inorganic Synthesis and Preparative Chemistry
College of Chemistry
Jilin University
Changchun 130012, P. R. China
E-mail: xxzou@jlu.edu.cn

R. Cao, G. Wan
Stanford Synchrotron Radiation Lightsource
SLAC National Accelerator Laboratory
Stanford University
Menlo Park, CA 94025, USA

W. Yan
National Synchrotron Radiation Laboratory
University of Science and Technology of China
Hefei, Anhui 230029, P. R. China

Dr. Y. Liu
School of Physical and Mathematical Sciences
Nanyang Technological University
Singapore 637371, Singapore

The ORCID identification number(s) for the author(s) of this article can be found under https://doi.org/10.1002/adma.202001430.

The oxygen evolution reaction (OER) is an electrochemical process, on which many energy conversion/storage systems depend, such as electricity/light-driven water splitting and emerging electroreduction of nitrogen and carbon dioxide.[1–3] The OER, taking place at the anode in these systems, is always associated with considerable overpotentials and thereby large energy losses. Thus, facilitating the OER process with suitable electrocatalysts at the smallest possible overpotentials is one of the essential needs of next-generation electrochemical technologies. This requirement has motivated some theoretical and experimental studies on understanding the electrochemical activity of catalyst materials and rationalizing their activity trend.[4] These fundamental knowledge provides some activity descriptors (e.g., orbital occupancy and binding energy between active site and key intermediates)—the readily accessible structural/electronic factors that are strongly correlated with catalytic activity; and further accelerates the search for more active catalysts.[5–8] While some progress in recent years has been made in optimizing the OER activity, the trade-off between catalytic activity and structural stability (i.e., catalyst dissolution or corrosion) is still difficult to resolve, especially for acidic oxygen evolution electrocatalysis.[9–13] The inverse catalytic activity–structural stability relation as a general phenomenon has been well-established in several catalyst systems for the acidic OER, and is controlled by both the intrinsic properties and surface defects of catalysts. For example, IrO_2, the benchmark OER catalyst under acidic conditions, has lower catalytic activity but higher structural stability than RuO_2. Thus, a major challenge in acidic OER electrocatalysis lies in developing suitable strategies to simultaneously optimize catalytic activity and structural stability of the material.

To this end, we chose perovskite-type strontium iridate ($SrIrO_3$) as a model material. The $SrIrO_3$ thin film with self-reconstructed surfaces was reported recently to show the best specific catalytic activity for the acidic OER, in terms of catalytic currents normalized by the catalyst's surface area.[15] Nevertheless, this perovskite material is still in the predicament of activity-stability trade-off: its high catalytic activity at the

expense of its easy corrosion.[14] Additionally, until now $SrIrO_3$ can only be prepared in the forms of thin films supported on catalytically-inert perovskite substrates[15–17] and free-standing, micrometer-scaled particles.[18] As a result, this perovskite material typically suffers from low surface areas and limited available catalytic active sites, which are detrimental to transferring its good specific activity to a real electrocatalyst with high mass activity. Therefore, the ability to structurally optimize perovskite catalysts at the nanoscale is of vital importance in our pursuit to develop higher-performance OER catalysts with improved both activity and stability.

Herein, we report the alloying of catalytically inert $SrZrO_3$ (SZO) in $SrIrO_3$ (SIO) to generate a novel perovskite-type solid solution electrocatalyst for efficiently electrocatalyzing the acidic OER. The alloying strategy is found to exert multiple positive effects on bulk and surface properties of the material, including the reduction of catalyst size, the decrease of catalyst covalency, and the weakening of surface oxygen-binding ability. The synergetic optimization of bulk and surface properties makes this electrocatalyst exhibit excellent catalytic activity for OER yet show significantly inhibited surface cation dissolution.

We synthesize micrometer-sized SIO particles based on our recently-reported experimental procedures with some modifications,[18] and a series of continuous SZO-SIO solid-solution perovskites over the entire compositional range under the same conditions (see Figures S1 and S2 and Table S1 in the Supporting Information). The experimental details are provided in the Supporting Information. Among the samples we synthesize, the solid solution perovskite with a Zr:Ir atomic ratio of 1:2 is demonstrated to exhibit the optimum catalytic performance (see discussion later). So this particular perovskite material, denoted as SZIO hereafter, is studied primarily in this work.

Figure 1a shows X-ray diffraction (XRD) patterns of SZO, SIO, and SZIO. The SZIO has a similar XRD pattern with SZO and SIO, demonstrating its solid solution perovskite structure without other impurity phases. Further comparison of the XRD patterns reveals that SZIO shows a shift of diffraction peaks to the smaller diffraction angles compared with SIO (Figure S2, Supporting Information), demonstrating a slight expansion of perovskite framework after the SZO alloying. This phenomenon can be explained by the fact that the radius of Zr^{4+} ions (72 pm) is larger than that of Ir^{4+} ions (63 pm). Additionally, the XRD peaks of SZIO appear broader than those of SIO and SZO, indicating the smaller particle size of SZIO. The transmission electron microscopy (TEM) images (Figure 1b; Figure S3, Supporting Information) shows that the SZIO contains perovskite nanoparticles with an optimal distribution size of about 19 nm. In contrast, the particle sizes for SIO and SZO are found to be around 1 μm and 50–100 nm, respectively (Figures S4 and S5, Supporting Information). Such an alloying-induced grain refinement was also observed in other solid solution systems due to the modified crystal nucleation/growth behaviors.[19,20] The high-resolution TEM (HRTEM) image of SZIO, together with the fast Fourier transform (FFT) image, shows characteristic interplanar spacings of 0.289, 0.289, and 0.287 nm, which correspond to the $(\bar{1}21)$, (121), and (200) crystallographic planes of perovskite structure (Figure 1c). The elemental mapping images of SZIO show that the Sr, Zr, and Ir elements are homogeneously distributed over the sample (Figure S6, Supporting Information).

To get more microstructural information about iridium atoms in SZIO, we investigate this material by X-ray absorption spectroscopy (XAS). Figure 1d presents the Ir L_3 edge X-ray absorption near edge structure (XANES) spectra of SZIO and SIO, which arise from the electronic transition from occupied O 2p to empty Ir 5d states. The white-line energy position of SZIO shows a little weaker peak intensity compared to that of IrO_2, suggesting a slightly lower oxidation states of iridium in SZIO. The result is also supported by XPS analysis (Figure S7, Supporting Information), in which the Ir 4f XPS peaks of SZIO present slight shifts toward higher binding energy as compared with those of IrO_2.[21] An enlargement of the white lines (Figure 1d, inset) shows that SZIO gives a little lower peak position and weaker peak intensity than SIO, indicating a higher electron density at Ir sites in SZIO relative to SIO. Figure 1e presents the extended X-ray absorption fine structure (EXAFS) spectra of SZIO and SIO. The main peak assigned to Ir–O bond is observed for both SZIO and SIO, whereas the other peak associated with Ir–M bond (M = Zr and Ir) is only observed for SZIO. Similar local metal–metal bonding was also observed in defect-enriched perovskite systems.[22] Additionally, the weakened intensity of the first shell implies a lower coordination number (CN) of iridium in SZIO. To more specific, iridium has a CN of 4.4 for SZIO, which is lower than that of SIO (CN = 6) (Figure S8 and Table S2, Supporting Information). The above results overall demonstrate that the alloying of SZO in SIO significantly changes not only the geometric dimension but also the microstructural environment of the material, and the resulting SZIO is such a nanomaterial that possesses some coordinatively unsaturated iridium sites and oxygen vacancies as well as serious local structural distortions (Figure 1f).

Next, we investigate the electrocatalytic activities for OER of SZO-SIO solid-solution perovskites with different Zr:Ir molar ratios in acidic media (see detailed electrochemical measurements in the Supporting Information). As shown in Figure S9 in the Supporting Information, the SZIO (Zr:Ir = 1:2) displays the highest electrocatalytic geometric activity (the measured current normalized by geometric area of the electrode) for OER among these SZO-SIO solid-solution perovskites. This result is also consistent with the analysis of Tafel plots in Figure S10 in the Supporting Information. Their intrinsic activities are further compared by normalizing the measured currents with pseudocapacitive charges (*Q*s), electrochemical surface areas (ECSAs), and Brunauer–Emmett–Teller (BET) surface areas in Figures S11–S16 in the Supporting Information. These comparison shows that the intrinsic activity of SZO-SIO solid-solution perovskite increases with the Zr:Ir atomic ratio to a maximum at 1:2, beyond which the electrocatalytic activity for OER begins to decrease. The above results overall demonstrate that the solid solution perovskite with a Zr:Ir atomic ratio of 1:2 (i.e., SZIO) is the most active catalytic material among the samples we synthesize.

In order to further evaluate the acidic OER performance of SZIO, SZO, SIO, and IrO_2 are also studied as the reference materials. **Figure 2**a shows their polarization curves for OER. As expected, SZO is totally inert, and other iridium-containing materials exhibit considerable catalytic activities for OER. For instance, SZIO gets a geometric current density (the current normalized by geometric area of the electrode) of 75 mA cm_{geo}^{-2}

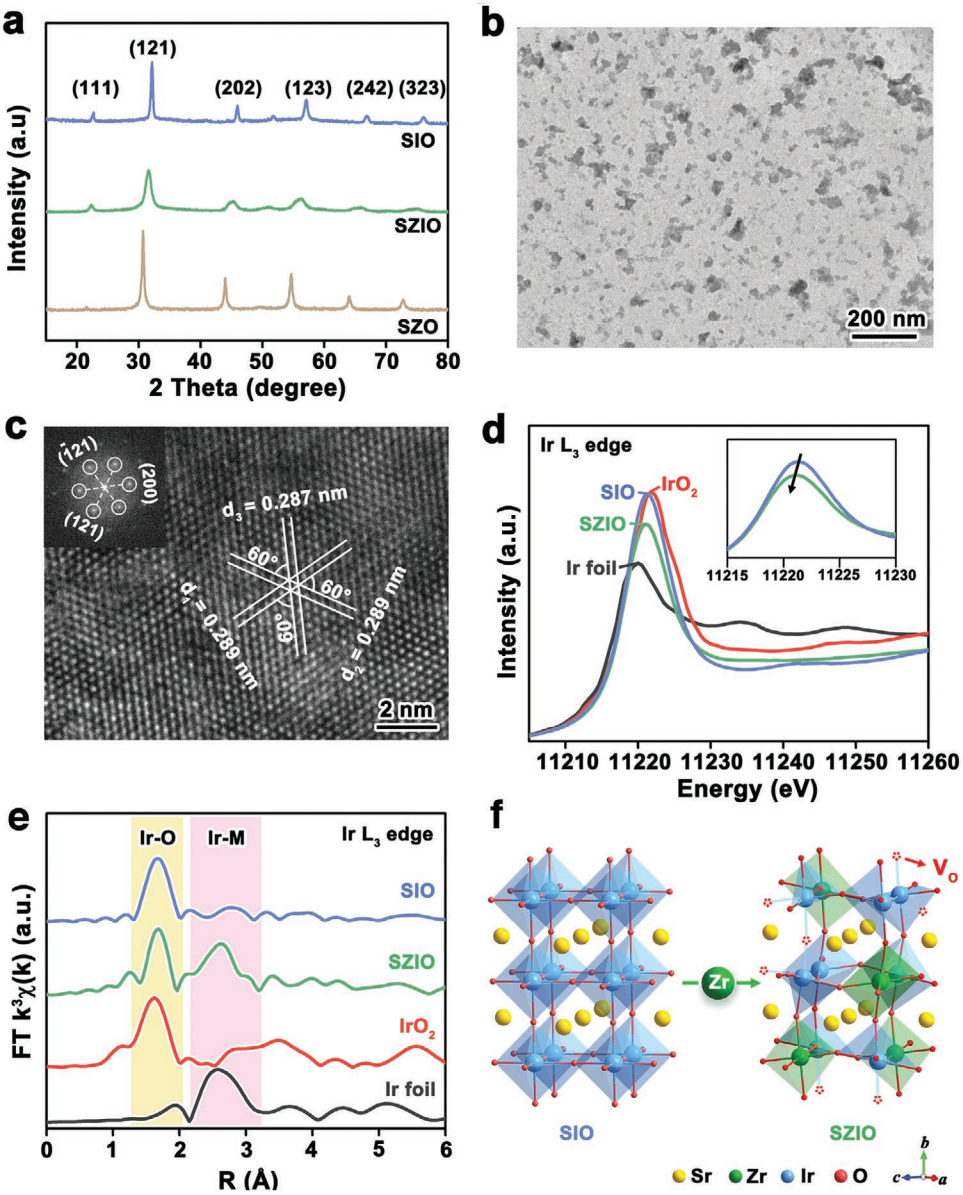

Figure 1. a) XRD patterns of SZO, SZIO, and SIO. b) TEM image of SZIO. c) HRTEM image of SZIO. Inset: the corresponding FFT image. d) XANES spectra of Ir foil, SZIO, SIO, and IrO_2. Inset: the enlargement of the white lines of SZIO and SIO. e) Fourier transform of K^3-weighted Ir L_3 edge EXAFS spectra of Ir foil, SZIO, SIO, and IrO_2. f) Schematic illustration the structures of SIO and SZIO.

at 1.53 V (or 300 mV overpotential), which is almost three and fifteen times higher than those of SIO and IrO_2, respectively. This result reveals that the alloying of inactive SZO significantly enhances the apparent oxygen evolution activity of SIO. SZIO and SIO give the smaller Tafel slopes of 43 mV dec^{-1} than IrO_2 (63 mV dec^{-1}), supporting their better OER activities than the latter (Figure S17, Supporting Information). The Tafel slopes around 40 mV dec^{-1} for SZIO and SIO suggest that their rate-determining step is the transformation from adsorbed OH specie to adsorbed O specie: M-OH → M-O + H^+ + e^-, where M stands for the active site. The Tafel slope of IrO_2 around 60 mV dec^{-1} corresponds to the rate-determining step that involves the water adsorption to form adsorbed OH specie and the successive energy optimization: M + H_2O → M-OH + H^+ + e^-.[23] Additionally, we compare the apparent catalytic activity of SZIO with some existing, highly efficient iridium-based oxygen evolution catalysts, based on the required overpotential (η) at 10 mA cm_{geo}^{-2}. As shown in Figure 2b, SZIO requires a lower overpotential (240 mV) to achieve 10 mA cm_{geo}^{-2} current density than most of other previously-reported Ir-containing oxygen evolution materials, including nanostructured metallic iridium-based catalysts[24–31] and oxide-type catalysts with various crystal structures.[18,32–39] Besides the apparent catalytic activity, the iridium mass activity (evaluated at a potential of 1.53 V) of SZIO is also compared with the previously-reported, representative catalysts. As shown in Figure 2c, SZIO gives an iridium mass activity of 1540 A g_{Ir}^{-1}, which is about thirty-nine times higher than that (39 A g_{Ir}^{-1}) of IrO_2 and

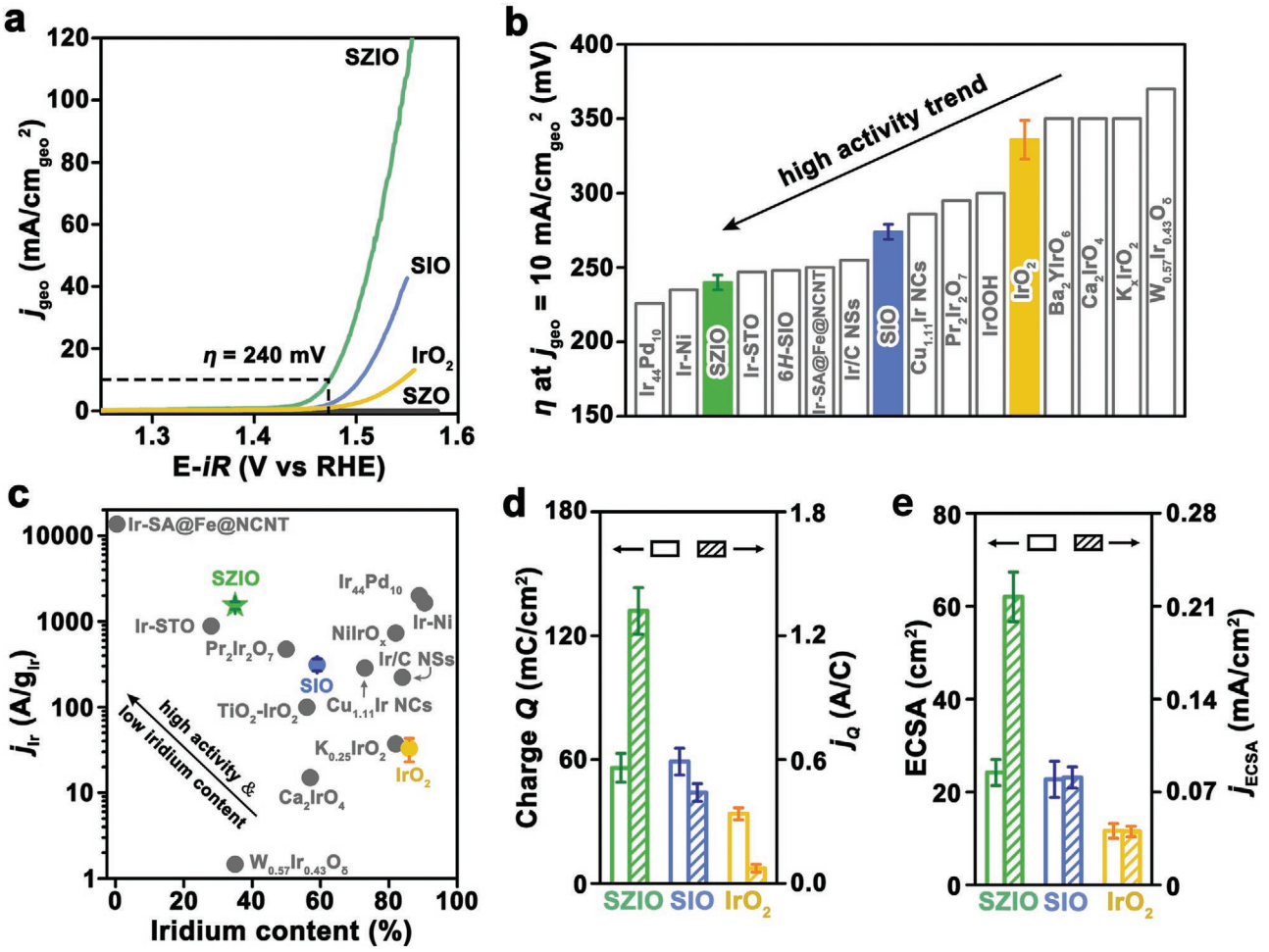

Figure 2. a) Polarization curves for OER of SZIO, SIO, SZO, and IrO_2 in 0.1 M $HClO_4$ solution. The current densities (j_{geo}) are normalized by the geometric area of the electrode. b) Comparison of overpotentials (η) required by SZIO and some representative iridium-based catalysts at 10 mA cm_{geo}^{-2}. c) Comparison of iridium mass activities (j_{Ir}) of iridium-based catalytsts at a potential of 1.53 V. The j_{Ir} of Ir-SA@Fe@NCNT and $Ir_{44}Pd_{10}$ are measured at 1.5 and 1.48 V, respectively. The *x*-axis is iridium content (wt%) in the catalyst. d) Comparison of pseudocapacitive charges (Q) and current densities (j_Q) normalized by Qs for SZIO, SIO, and IrO_2. e) Comparison of electrochemical surface areas (ECSA) and current densities (j_{ECSA}) normalized by ECSAs for SZIO, SIO, and IrO_2. The error bars in (b)–(e) represent standard deviations based on five measurements.

nearly five times as high as that (314 A g_{Ir}^{-1}) of SIO. In addition, while the majority of the existing catalysts give an iridium mass activity below 500 A g_{Ir}^{-1},[32–40] only three ones (including Ir-based single-atom catalyst and nanostructured metallic Ir-based alloys)[29–31] exhibit higher iridium mass activity than SZIO. The results overall demonstrate that SZIO is among the most active Ir-based electrocatalysts for OER under acidic conditions.

In order to assess the intrinsic activity of iridium sites, we measure pseudocapacitive charges (Qs) and ECSAs of SZIO, SIO, and IrO_2 (Figures S11d,f,g and S13d,f,g, Supporting Information), and then normalize the currents with respect to Qs and ECSAs, respectively. Both the Qs and ECSAs follow the trend of SZIO ≈ SIO > IrO_2 (Figure 2d,e). The similar Qs and ECSAs for SZIO and SIO imply that compared to SIO, the positive nanostructuring effect for SZIO compensates the negative influence from the decrease in absolute iridium content in terms of the available catalytic sites. Figure 2d,e also shows that the intrinsic activity of iridium sites increases in the order: SZIO > SIO > IrO_2. The above results further suggest that the alloying of catalytically inert SZO in SIO yields more active Ir-based catalytic sites for OER; and the enhancement of intrinsic activity of iridium sites is one of the main reasons for rationalizing the excellent oxygen-evolution catalytic activity of SZIO.

In addition to high catalytic activity, the SZIO also shows good catalytic stability for the acidic OER. As shown in **Figure 3**a, after 1000-cycle cyclic voltammetry (CV) testing, the SIO gives a decrease in current density by 17%, whereas the SZIO affords almost the same linear sweep voltammetry (LSV) curve as before. This is further confirmed by the chronopotentiometric testing results (Figure S18, Supporting Information). The SZIO retains its catalytic activity over thirty hours at 10 mA cm_{geo}^{-2} current density, which is more catalytically stable in comparison with SIO. These results suggest that the alloying of SZO in SIO can improve the catalytic stability for OER in acidic solution.

We also investigate the structural stability of SZIO after OER by various characterization methods. The XRD pattern and X-ray photoelectron spectra (XPS) for Zr 3d and Ir 4f

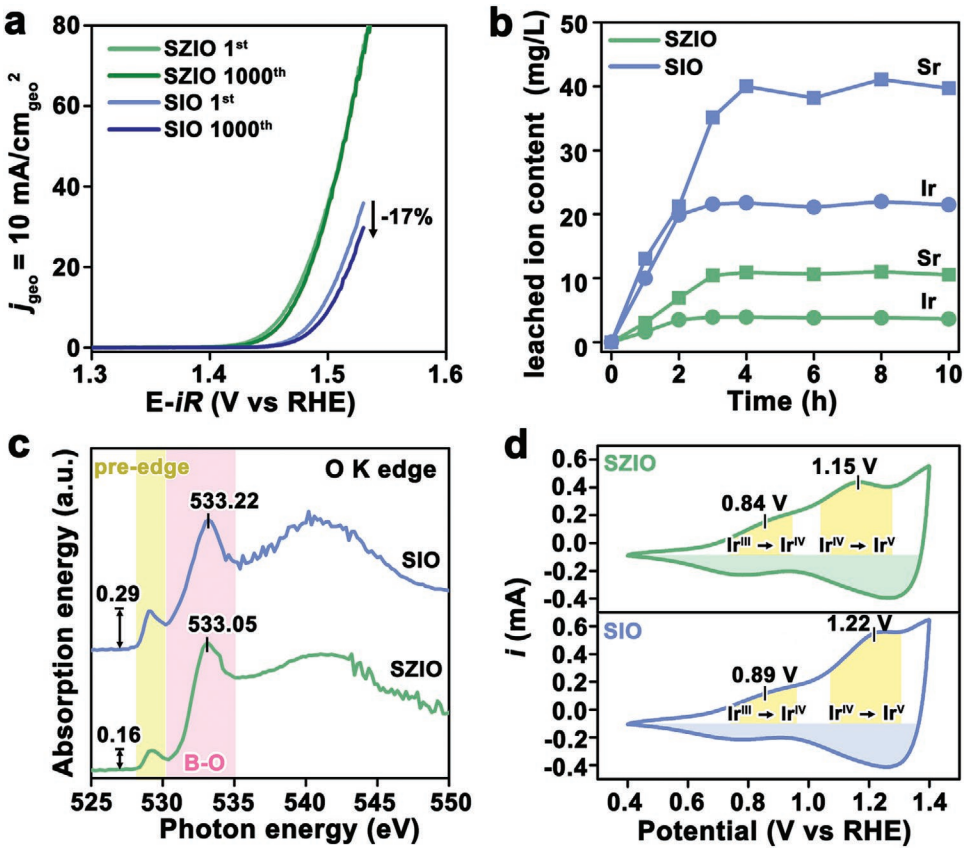

Figure 3. a) LSV curves obtained with SZIO and SIO before and after 1000 CV cycles. b) Contents of leached metals in the electrolyte in the presence of SZIO and SIO during 10 h long electrocatalysis. c) Normalized O K edge XAS spectra of SZIO and SIO. d) CV curves obtained with SZIO and SIO between 0.4 and 1.4 V vs RHE.

(Figures S19–S21, Supporting Information) show that the SZIO maintains its perovskite structure as well as the oxidation states of Zr and Ir after OER. But the Sr 3d XPS spectrum (Figure S22, Supporting Information) exhibits an observable decrease in the intensity of XPS peaks, indicating the Sr leaching during the OER process. And the HRTEM images (Figure S23, Supporting Information) reveal that there is an amorphous thin layer (1–2 nm) around the SZIO particles after OER. The leached amounts of cations during OER are quantitatively determined by inductively coupled plasma atomic emission spectroscopy (ICP-OES). As shown in Figure 3b, for the SZIO there are no detectable leached Zr species in the electrolyte, but Sr and Ir dissolusions increase steadily at the first three hours and then become constant. The constant concentrations of Sr and Ir ions in the electrolyte are 10.9 and 3.9 mg L^{-1}, respectively. The cation leaching for SZIO is much weaker than that for SIO, which gives constant Sr and Ir concentrations of 40.0 and 21.8 mg L^{-1}, respectively, in the electrolyte. This comparison suggests that the alloying of SZO in SIO markedly enhances the structural stability of the latter. The stability of SZIO was further evaluated by stability number (S-number), according to the method proposed by Gieger et al.[14] The result in Figure S24 (Supporting Information) shows that SZIO has a similar S-number with IrO_2 during OER. These stability studies, together with the earlier discussion on catalytic activity, overall demonstrate that the alloying strategy is an effective method for simultaneous improvement of catalytic activity and structural stability of perovskite-type OER electrocatalysts.

To rationalize the difference in structural stability, we study the O K-edge X-ray absorption spectra of SZIO and SIO (Figure 3c). The pre-edge feature (the region before 530 eV) is ascribed to the electronic transition from the O 1s core level to the unoccupied O 2p states hybridized with Ir 5d orbitals. The absorption peak at 530–535 eV is associated with the hybridization of M d orbitals and O 2p orbitals (M = Zr and Ir). When SIO alloyed with SZO, the normalized intensity of the pre-edge peak decreases and the energy position of M–O hybridization shifts negatively (Figure 3c). This result, together with recent studies on perovskite catalysts,[18] suggests that the SZO-SIO alloying results in a weaker metal–oxygen covalency in the perovskite framework of SZIO, and thereby benefits the inhibition of surface cation dissolution.

We finally explore the fundamental reasons responsible for the improved intrinsic activity of iridium sites for SZIO. Although the coordinatively unsaturated iridium sites exist in SZIO before the OER (Figure 1), they become coordinatively saturated as the OER progresses and simultaneously the catalytic activity of SZIO keeps almost unchanged (Figure S25 and Table S3, Supporting Information). This result demonstrates that the coordinatively unsaturated Ir sites, observed in the material before OER, cannot account for the superior intrinsic activity of iridium sites for SZIO. We further investigate the

electrochemical redox properties of SZIO and SIO by cyclic voltammetry. As shown in Figure 3d, two couples of redox peaks can be observed during the OER process between 0.4 and 1.4 V versus RHE for both SZIO and SIO.[41] The first oxidation peak located at 0.84 V is ascribed to the oxidation of Ir^{3+} to Ir^{4+}, according to the Equation (1)

$$Ir^{3+}(OH)_x \rightarrow Ir^{4+}O(OH)_{x-1} + H^+ + e^- \quad (1)$$

and the second oxidation peak at 1.15 V originates from the oxidation of Ir^{4+} to Ir^{5+}, according to the Equation (2)

$$Ir^{4+}O(OH)_{x-1} \rightarrow Ir^{5+}O_2(OH)_{x-2} + H^+ + e^- \quad (2)$$

Compared with those for SIO, the two oxidation peaks for SZIO appear at lower potentials. This observation indicates that the presence of redox-inactive SZO constituent in SZIO facilitates the generation of high-valent iridium sites, probably allowing to mediate the OER more efficiently.

To gain further insight into the catalytic activity of Ir sites for SZIO, we perform density functional theory (DFT) calculations. In view of our experimental observation on the Sr-deficient surface of SZIO during the OER and the recent theoretical study on the SIO catalyst by Seitz et al.,[15] we establish the theoretical model ($Ir(Zr)O_2$/SZIO) with a perovskite SZIO core covered with an anatase-type $Ir(Zr)O_2$ shell (see theoretical details in the Supporting Information). Similarly, a shell/core IrO_2/SIO model is also established (Figure S26, Supporting Information). There are two possible exposed surfaces for $Ir(Zr)O_2$/SZIO, which are labeled as Surface-a (**Figure 4**a) and Surface-b (Figure S27a, Supporting Information). Surface phase diagrams (Figure 4b; Figure S27b, Supporting Information) for both Surface-a and Surface-b prefer to be covered with HO species in the interesting potential range for OER (i.e., >1.23 V vs RHE).

All theoretical overpotentials for OER of the exposed metal sites on Surface-a and Surface-b are listed in Figure 4c. The overpotentials (>0.76 V) for all the Zr sites on Surface-a and Surface-b are too high, indicating that the Zr sites are catalytically inactive for OER. The overpotantials for the Ir1, Ir2, Ir3, Ir4, and Ir5 sites are 0.48, 0.40, 0.37, 0.42, and 0.74 V, respectively. The overpotentials of the exposed Ir sites on Surface-a and Surface-b, except the Ir5 site, are smaller than that of Ir sites (0.55 V) for the IrO_2/SIO model. This result demonstrates that the Ir sites for $Ir(Zr)O_2$/SZIO, in general, have better catalytic activity toward OER than those for IrO_2/SIO, in agreement with our experimental results.

The bonding and antibonding characters between the surface Ir sites (e.g., Ir2) and the adsorbed oxygen intermediate (O_{ads}) are studied through crystal orbital hamiltonian population

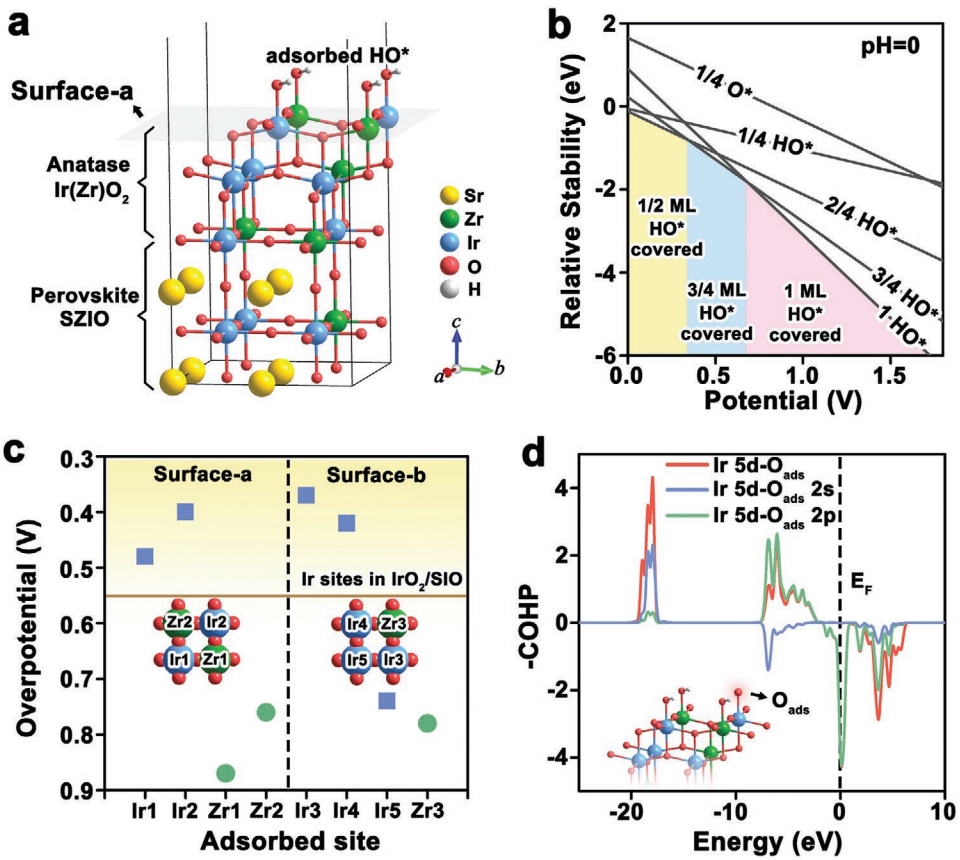

Figure 4. a) The theoretical model of $Ir(Zr)O_2$/SZIO. The Surface-a is highlighted in the model. b) The surface phase diagram for the Surface-a. c) The theoretical overpotentials for OER of all the Ir and Zr sites on Surface-a and Surface-b. Top views of Surface-a and Surface-b, with the corresponding Ir and Zr sites, are shown. d) Crystal Orbital Hamiltonian Population (COHP) for the Ir-O_{ads} bond in SZIO. The Fermi level (E_F) is set to 0. The inset shows the structural model Surface-a with the oxygen adsorption at the Ir2 site.

(COHP). As shown in Figure 4d, both of bonding (expressed by the positive -COHP value) and antibonding (expressed by the negative -COHP value) of Ir 5d-O_{ads} 2s orbitals are mainly below Fermi level. In contrast, the bonding interaction for Ir 5d-O_{ads} 2p orbitals is mainly below Fermi level, but its antibonding interaction is above Fermi level. This result suggests that the hybridization between Ir 5d orbitals and O_{ads} 2p orbitals has a dominant role in the surface adsorption of the oxygen-containing intermediates. Moreover, the integrated COHP value of Ir 5d-O_{ads} 2p orbital hybridization for Ir2 is –4.49 eV, which is bigger than that (–4.68 eV) for the IrO_2/SIO model. This result demonstrates that the Ir2 site has a weaker oxygen binding ability, which leads to a moderate adsorption interaction and could be the fundamental cause of the enhanced intrinsic catalytic activity of iridium sites for the solid solution catalysts.

In summary, the importance of synergistic optimization of bulk and surface properties for breaking inverse relation of catalytic activity and structural stability of OER electrocatalyst, with $SrIrO_3$ as a model material, has been demonstrated. An alloying strategy is presented to achieve this goal, and results in a high-performance $SrZrO_3$–$SrIrO_3$ solid-solution electrocatalyst for the acidic OER. Our findings could encourage the further development of better oxygen evolution electrocatalysts, with balanced activity and stability.

Acknowledgements

X.Z. thanks the support from National Key R&D Program of China, Grant No. 2017YFA0207800 and NSFC Grant No. 21922507. The authors also thank the NSFC Grant No. 21621001 and the 111 Project No. B17020 for financial support. The authors thank BL12B-a of National Synchrotron Radiation Laboratory (NSRL) in China for providing the beam time. This research used resources of Stanford Synchrotron Radiation Lightsource (SSRL), SLAC National Accelerator Laboratory, is supported by the U.S. Department of Energy, Office of Science, Office of Basic Energy Sciences under Contract No. DE-FOA-0000559. R.C. acknowledges the support from DOE funded LDRD program and SSRL.

Conflict of Interest

The authors declare no conflict of interest.

Keywords

alloying, electrocatalysis, iridium, oxygen evolution reaction, solid solution

Received: February 28, 2020
Revised: June 27, 2020
Published online:

[1] L. Han, S. Dong, E. Wang, *Adv. Mater.* **2016**, *28*, 9266.
[2] B. M. Hunter, H. B. Gray, A. M. Müller, *Chem. Rev.* **2016**, *116*, 14120.
[3] Y. Jiao, Y. Zheng, M. Jaroniec, S. Z. Qiao, *Chem. Soc. Rev.* **2015**, *44*, 2060.
[4] Z. W. She, J. Kibsgaard, C. F. Dickens, I. Chorkendorff, J. K. Nørskov, T. F. Jaramillo, *Science* **2017**, *355*, eaad4998.
[5] J. Suntivich, K. J. May, H. A. Gasteiger, J. B. Goodenough, Y. Shao-Horn, *Science* **2011**, *334*, 1383.
[6] R. Subbaraman, D. Tripkovic, K. C. Chang, D. Strmcnik, A. P. Paulikas, P. Hirunsit, M. Chan, J. Greeley, V. Stamenkovic, N. M. Markovic, *Nat. Mater.* **2012**, *11*, 550.
[7] A. Grimaud, K. J. May, C. E. Carlton, Y. L. Lee, M. Risch, W. T. Hong, J. Zhou, Y. Shao-Horn, *Nat. Commun.* **2013**, *4*, 2439.
[8] F. Calle-Vallejo, O. A. Díaz-Morales, M. J. Kolb, M. T. M. Koper, *ACS Catal.* **2015**, *5*, 869.
[9] N. Danilovic, R. Subbaraman, K. C. Chang, S. H. Chang, Y. Kang, J. Snyder, A. P. Paulikas, D. Strmcnik, Y. T. Kim, D. Myers, V. R. Stamenkovic, N. M. Markovic, *Angew. Chem., Int. Ed.* **2014**, *53*, 14016.
[10] N. Danilovic, R. Subbaraman, K. C. Chang, S. H. Chang, Y. J. Kang, J. Snyder, A. P. Paulikas, D. Strmcnik, Y. T. Kim, D. Myers, V. R. Stamenkovic, N. M. Markovic, *J. Phys. Chem. Lett.* **2014**, *5*, 2474.
[11] C. Spöri, J. T. H. Kwan, A. Bonakdarpour, D. P. Wilkinson, P. Strasser, *Angew. Chem., Int. Ed.* **2017**, *56*, 5994.
[12] X. Rong, J. Parolin, A. M. Kolpak, *ACS Catal.* **2016**, *6*, 1153.
[13] Y. Lin, Z. Tian, L. Zhang, J. Ma, Z. Jiang, B. J. Deibert, R. Ge, L. Chen, *Nat Commun.* **2019**, *10*, 162.
[14] S. Geiger, O. Kasian, M. Ledendecker, E. Pizzutilo, A. M. Mingers, W. T. Fu, O. Diaz-Morales, Z. Li, T. Oellers, L. Fruchter, A. Ludwig, K. J. J. Mayrhofer, M. T. M. Koper, S. Cherevko, *Nat. Catal.* **2018**, *1*, 508.
[15] L. C. Seitz, C. F. Dickens, K. Nishio, Y. Hikita, J. Montoya, A. Doyle, C. Kirk, A. Vojvodic, H. Y. Hwang, J. K. Nørskov, T. F. Jaramillo, *Science* **2016**, *353*, 1011.
[16] R. Tang, Y. Nie, J. K. Kawasaki, D. Y. Kuo, G. Petretto, G. M. Rignanese, K. M. Shen, D. G. Schlom, J. Suntivich, *J. Mater. Chem. A* **2016**, *4*, 6831.
[17] C. W. Song, H. Suh, J. Bak, H. B. Bae, S. Y. Chung, *Chem* **2019**, *5*, 3243.
[18] L. Yang, G. Yu, X. Ai, W. Yan, H. Duan, W. Chen, X. Li, T. Wang, C. Zhang, X. Huang, J. S. Chen, X. Zou, *Nat. Commun.* **2018**, *9*, 5236.
[19] Z. Liu, R. Li, R. Jiang, X. Li, M. Zhang, *J. Alloys Comp.* **2016**, *687*, 885.
[20] H. Chen, G. Yu, G. D. Li, T. Xie, Y. Sun, J. Liu, H. Li, X. Huang, D. Wang, T. Asefa, W. Chen, X. Zou, *Angew. Chem., Int. Ed.* **2016**, *55*, 11442.
[21] V. Pfeifer, T. E. Jones, J. J. Velasco Vélez, C. Massué, M. T. Greiner, R. Arrigo, D. Teschner, F. Girgsdies, M. Scherzer, J. Allan, M. Hashagen, G. Weinberg, S. Piccinin, M. Hävecker, A. Knop-Gerickea, R. Schlögl, *Phys. Chem. Chem. Phys.* **2016**, *18*, 2292.
[22] X. Wang, K. Huang, L. Yuan, S. Li, W. Ma, Z. Liu, S. Feng, *ACS Appl. Mater. Interfaces* **2018**, *10*, 28219.
[23] J. Park, Y. J. Sa, H. Baik, T. Kwon, S. H. Joo, K. Lee, *ACS Nano* **2017**, *11*, 5500.
[24] G. Wu, X. Zheng, P. Cui, H. Jiang, X. Wang, Y. Qu, W. Chen, Y. Lin, H. Li, X. Han, Y. Hu, P. Liu, Q. Zhang, J. Ge, Y. Yao, R. Sun, Y. Wu, L. Gu, X. Hong, Y. Li, *Nat. Commun.* **2019**, *10*, 4855.
[25] C. Wang, Y. Sui, G. Xiao, X. Yang, Y. Wei, G. Zou, B. Zou, *J. Mater. Chem. A* **2015**, *3*, 19669.
[26] Y. Pi, N. Zhang, S. Guo, J. Guo, X. Huang, *Nano Lett.* **2016**, *16*, 4424.
[27] Y. Pi, Q. Shao, P. Wang, J. Guo, X. Huang, *Adv. Funct. Mater.* **2017**, *27*, 1700886.
[28] J. Shan, T. Ling, K. Davey, Y. Zheng, S. Z. Qiao, *Adv. Mater.* **2019**, *31*, 1900510.
[29] F. Luo, H. Hu, X. Zhao, Z. Yang, Q. Zhang, J. Xu, T. Kaneko, Y. Yoshida, C. Zhu, W. Cai, *Nano Lett.* **2020**, *20*, 2120.

[30] J. Zhu, Z. Chen, M. Xie, Z. Lyu, M. Chi, M. Mavrikakis, W. Jin, Y. Xia, *Angew. Chem., Int. Ed.* **2019**, *58*, 7244.
[31] S. M. Alia, S. Shulda, C. Ngo, S. Pylypenko, B. S. Pivovar, *ACS Catal.* **2018**, *8*, 2111.
[32] X. Liang, L. Shi, Y. Liu, H. Chen, R. Si, W. Yan, Q. Zhang, G. D. Li, L. Yang, X. Zou, *Angew. Chem., Int. Ed.* **2019**, *58*, 7631.
[33] S. Kumari, B. P. Ajayi, B. Kumar, J. B. Jasinski, M. K. Sunkara, J. M. Spurgeon, *Energy Environ. Sci.* **2017**, *10*, 2432.
[34] E. Oakton, D. Lebedev, M. Povia, D. F. Abbott, E. Fabbri, A. Fedorov, M. Nachtegaal, C. Copéret, T. J. Schmidt, *ACS Catal.* **2017**, *7*, 2346.
[35] O. Diaz-Morales, S. Raaijman, R. Kortlever, P. J. Kooyman, T. Wezendonk, J. Gascon, W. T. Fu, M. T. Koper, *Nat. Commun.* **2016**, *7*, 12363.
[36] C. Shang, C. Cao, D. Yu, Y. Yan, Y. Lin, H. Li, T. Zheng, X. Yan, W. Yu, S. Zhou, J. Zeng, *Adv. Mater.* **2019**, *31*, 1805104.
[37] D. Weber, L. M. Schoop, D. Wurmbrand, S. Laha, F. Podjaski, V. Duppel, K. Muller, U. Starke, B. V. Lotsch, *J. Mater. Chem. A* **2018**, *6*, 21558.
[38] J. Kim, P. C. Shih, Y. Qin, Z. Al-Bardan, C. J. Sun, H. Yang, *Angew. Chem., Int. Ed.* **2018**, *57*, 13877.
[39] A. Grimaud, A. Demortière, M. Saubanère, W. Dachraoui, M. Duchamp, M. L. Doublet, J. M. Tarascon, *Nat. Energy* **2016**, *2*, 16189.
[40] H. N. Nong, T. Reier, H. S. Oh, M. Gliech, P. Paciok, T. H. T. Vu, D. Teschner, M. Heggen, V. Petkov, R. Schlögl, T. Jones, P. Strasser, *Nat. Catal.* **2018**, *1*, 841.
[41] Z. Pavlovic, C. Ranjan, Q. Gao, M. Gastel, R. Schlögl, *ACS Catal.* **2016**, *6*, 8098.